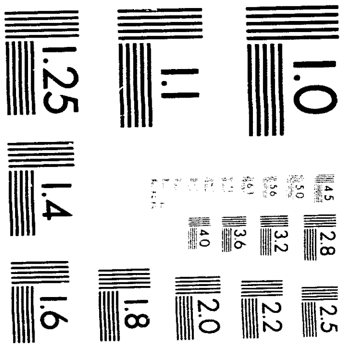
1.0
1.1
1.25
1.4
1.6
1.8
2.0
2.2
2.5
2.8
3.2
3.6
4.0
4.5
5.0
5.6

1 of 1

SAND 93-1588
Unlimited Release
August 1993

Distribution
Category UC-404

Flow and Heat Transfer Model for a Rotating Cryogenic Motor

R. C. Dykhuizen and R. G. Baca, 1513 and T. C. Bickel, 6213
Energy and Environment Division
Sandia National Laboratories
Albuquerque, New Mexico 87185

Abstract

Development of a high-temperature, superconducting, synchronous motor for large applications (>1000 HP) could offer significant electrical power savings for industrial users. Presently 60% of all electric power generated in the United States is converted by electric motors. A large part of this power is utilized by motors 1000 HP or larger. The use of high-temperature superconducting materials with critical temperatures above that of liquid nitrogen (77 K) in the field winding would reduce the losses in these motors significantly, and therefore, would have a definite impact on the electrical power usage in the U.S. These motors will be 1/3 to 1/2 the size of conventional motors of similar power and, thus, offer potential savings in materials and floor space.

The cooling of the superconducting materials in the field windings of the rotor presents a unique application of cryogenic engineering. The rotational velocity results in significant radial pressure gradients that affect the flow distribution of the cryogen. The internal pressure fields can result in significant nonuniformities in the two-phase flow of the coolant. Due to the variable speed design, the flow distribution has the potential to change during operation.

A multiphase-flow computer model of the cryogenic cooling is developed to calculate the boiling heat transfer and phase distribution of the nitrogen coolant in the motor. The model accounts for unequal phase velocities and nonuniform cooling requirements of the rotor. The unequal radial pressure gradients in the inlet and outlet headers result in a larger driving force for flow in the outer cooling channels. The effect of this must be accounted for in the design of the motor. Continuing improvements of the model will allow the investigation of the transient thermal issues associated with localized quenching of the superconducting components of the motor.

Table of Contents

Acknowledgment

This work was performed under the sponsorship of the Superconductivity Technology Program in the Office of Utility Technology of the U.S. DOE. In addition, we acknowledge the assistance of Reliance Electric supported by the Electric Power Research Institute in the definition of the model parameters.

1. Introduction

Sandia National Laboratories is developing a thermal analysis of the cryogenic cooling of a high-temperature superconducting (HTS) motor. The Reliance Electric design, a 5000 hp synchronous motor with copper armature windings and HTS field windings is being developed under contract with the Electric Power Research Institute. Development of such a motor could offer significant electrical power savings for industrial users, and material cost savings to the manufacturers. As HTS materials and the Reliance Electric design have evolved, the heat load distribution within the motor has changed from electrical losses that typically must be removed from traditional motor designs to thermal heat leaks into the proposed HTS cryogenic motor design. The majority of the thermal load is expected to result from thermal conduction along the torque tube from the ambient environment to the liquid-nitrogen temperature (77 K) field windings. This results in very localized heat sources. Anisotropic internal conduction distributes the heat load non-uniformly throughout the rotor.

The cooling of the superconducting field winding of the rotor presents a unique application of cryogenic engineering. The rotational velocity of the rotor (design operating range of 1800-3600 rpm) results in significant radial pressure gradients that strongly affect the two-phase flow distribution of the cryogen. A multiphase-flow computer model of the cryogenic cooling system is being developed to predict the boiling heat transfer and phase distribution of the cryogen in the rotor. The model accounts for unequal phase velocities and nonuniform cooling requirements within the rotor.

2. Rotor Geometry

Figure 1 shows a simplified cross-section view of the 5000 hp rotor assembly. Cryogen enters the rotor through a transfer coupling and flows axially through a hollow shaft. The cryogen (sub-cooled liquid nitrogen in this case) enters the transfer coupling at a given pressure. Pressure drop from the transfer coupling to the rotor inlet header is ignored, however, the cryogen's energy content increases due to heat leaks in the transport piping. Cryogen enters the inlet header on the torque-output side of the motor. The inlet header feeds axial channels that cool the rotor rotating at a synchronous speed between 1800 and 3600 rpm. The nitrogen flows through these channels, cools the rotor, and exits via a common outlet header.

Due to the rotational acceleration, the fluid pressure increases with radius in each of the headers. Since the fluid density will not be equal in the two headers (due to the heating of the fluid as it passes through the rotor), the rates of increase with radius are not equal. This results in a nonuniform cryogen flow distribution in the axial channels of the rotor. Thus, it is important to model the various heat leak terms, and the electrical power losses, to determine fluid densities as a function of radial position in the two headers. Small density differences cause the rotor to be self pumping; Flow will occur even if no pressure drop across the rotor is imposed.

A number of basic concerns were identified by examining the unique flow geometry of Figure 1:

- The high acceleration fields might affect the flow regimes in the axial channels. This will affect the heat transfer coefficient and the pressure drop/flow relation. At this point, models that account for the effect of the acceleration field on the axial flow channels have not been developed. Due to the large pressures generated by the rotational motion, boiling only occurs in the central channels.

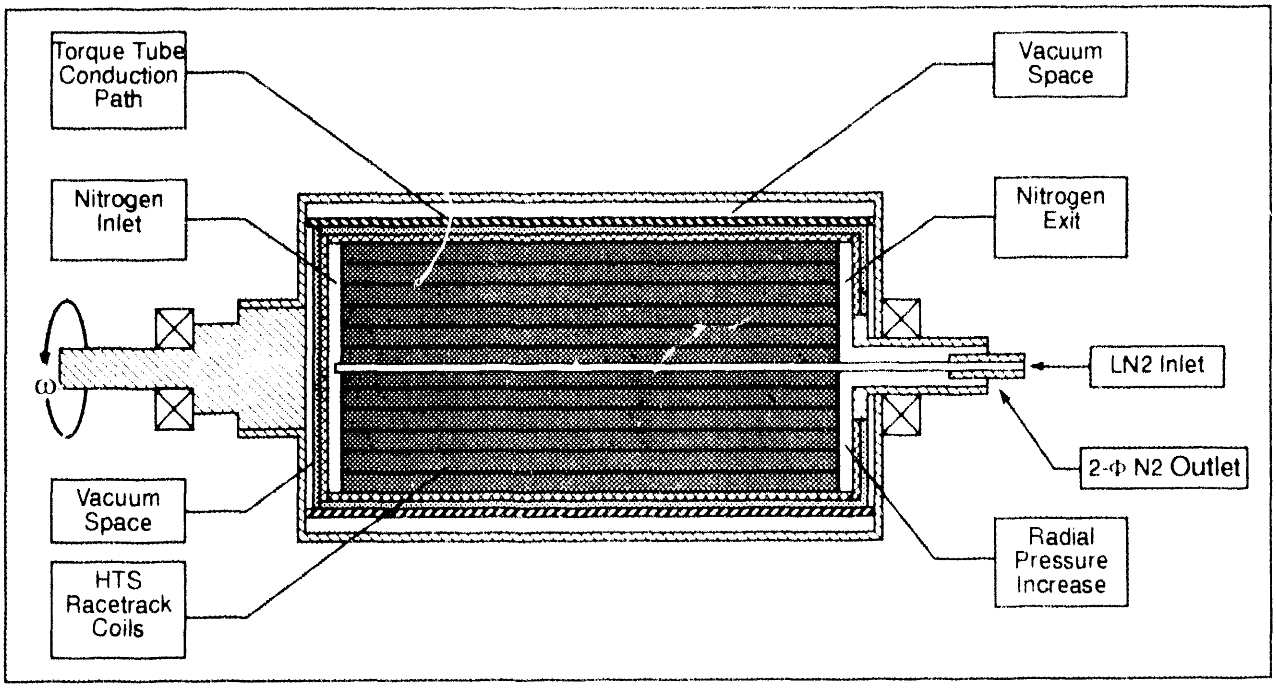

Figure 1. Simplified geometry of the cryogenic rotor for a 5000-hp synchronous motor. Liquid nitrogen enters on the right, passes through the rotor center, is distributed radially in the inlet header, then flows axially back through the field winding. Liquid and vapor nitrogen are collected in the outlet header and exhausted.

- Conservation of angular momentum requires that the fluid rotating in the outlet header increase its rotational velocity as it is drawn towards the outlet. This results in a very complex flow since wall shear forces will tend to retard this acceleration. We currently model the flow assuming radial vanes are placed in both headers to force the fluid to rotate with the header walls at a fixed angular velocity. The vanes will result in a retarding torque on the motor at the inlet, but it will be partially balanced by an assisting torque at the outlet header. These vanes force the flow to become more amenable to modeling (since the tangential velocity is fixed by the vanes); thus the model will become more useful to guide prototype designs. Eckman layer flows (Greenspan, 1968) that would exist in this steady rotating geometry are also eliminated by the radial vanes.

- The pressure history at a point in the headers will vary periodically due to the rotation of the rotor. Assuming that the motor axis is horizontal, lower pressures will be experienced at positions above the inlet (due to a gravitational head), and the opposite will be true for positions below the inlet. The following equation can be used to estimate the local pressure as a function of time, t, for a point at radius, r, in the inlet header (assuming negligible friction):

$$P_l(r,t) = P_{inlet} + \frac{\rho_l r^2 \omega^2}{2} + \rho_l g r \sin(\omega t) . \qquad (1)$$

If a ratio is made of the time-varying portion of the local pressure (Equation (1)) to the average local pressure, it is found that this ratio reaches a maximum at:

$$P_{inlet} - \frac{1}{2}\rho_f\omega^2 r^2 = 0 \qquad (2)$$

For a 3600 rpm operating point, this maximum occurs at r = 0.042 m. At this point the contribution of the time-varying term of Equation (1) is only 0.2% of the mean pressure. For this reason, and because boiling systems are inherently noisy, the time-varying contribution to the pressure head was not included.

- Finally, the rotor consists of a number of parallel boiling channels between common headers. This situation is conducive to boiling flow instabilities (Bergles, 1981; Miropolsky and Soziev, 1990). A density wave instability causes the flow rate in a particular axial channel to oscillate. However, the thermal powers, and thus the exit qualities are very low in the central channels where boiling is possible. Therefore, these classic instabilities are unlikely.

3. Model Formulation

A model of the flow through the rotor is presented here. The five ordinary differential equations presented as the basis of the model describe the radial changes in the headers. The axial flow of cryogen through the rotor is introduced via constitutive relations. The following variables are chosen as the state variables of the system (Note a nomenclature section at the end of this report defines all variables used.):

P_i	the inlet header pressure
P_o	the outlet header pressure
F	the radial mass flow rate in the headers (this will be the same function for both)
h_i	the inlet manifold enthalpy
h_o	the outlet manifold enthalpy

All of the five state variables above are a function of the radial coordinate. Boundary conditions or energy balances will fix all of the state variables at the inner radius of each header. Defining initial values for the state variables at the inner radius allows the integration of the state equations as an initial value problem. Unfortunately, it is not possible to define an initial condition for all of the state variables. The problem is over-specified if the two pressures and the flow are imposed. Therefore a shooting method is derived for the flow rate. In presenting the equations, it will be assumed that all five state variables are known at the inner radius. The flow rate is updated after each iteration based on the solutions obtained from the previous iteration. During each iteration the temperature field is also updated. The changing temperature field also affects the flow distribution within the rotor.

The five governing differential equations are introduced here. The first two represent mixture momentum equations in the two headers. In deriving these equations it is assumed that the frictional pressure drop is negligible due to the low radial velocity through the headers:

$$\frac{dP_i}{dr} = \rho_i\omega^2 r \qquad (3)$$

$$\frac{dP_o}{dr} = \rho_o\omega^2 r, \qquad (4)$$

Note that the inlet and outlet header densities (ρ_i and ρ_o) in the above two equations are a function of the local state variables (P and h). The exit header contains two-phase regions. Therefore, the densities are also dependent upon the slip velocity between the phases. A model is later introduced to determine the mixture density in the headers.

The axial channels in the rotor are distributed in a rectangular grid around the HTS material regions in the proposed Reliance Electric design. However, the model developed here is axisymmetric for ease of solution. Therefore, the location of the axial channels are assumed to be grouped in a number of sets, each at a constant radius. For the results presented here, each radial group of channels is one centimeter apart. The radial mass flow in the headers decreases incrementally as the radial coordinate increases past the location of the axial channels. At these locations the enthalpy of the header and the radial flow rate changes in a discontinuous fashion. The pressure level continues to change continuously as the channel locations are passed. Therefore, the state equations are integrated between the axial channel radial locations, and then the flow rate and enthalpy of the flows are adjusted to account for the flow through the channels. The governing equation for the radial flow in the headers is:

$$\frac{dF}{dr} = 0. \tag{5}$$

The final two differential equations can be derived from energy balances for the flow in the two headers:

$$\frac{dh_i}{dr} = \omega^2 r + \frac{2\pi r q''_i}{F} \tag{6}$$

and

$$\frac{dh_o}{dr} = \omega^2 r - \frac{2\pi r q''_o}{F}. \tag{7}$$

The variables q''_i and q''_o represent the axial heat leak fluxes into the inlet and outlet headers respectively.

Discontinuous changes at the radial locations of axial channels

As the radial location of the axial channels are reached, the integration of the above equations are stopped, and the radial flow rate is reduced by the flow passed through the axial channels. Energy balances are also used to determine changes in the enthalpy of the radial flows. The pressure remains continuous at these radial locations. The following mass and energy balances are used.

$$F(r+\ ) = F(r-\ ) - N(r)\,w(r) \tag{8}$$

$$h_i(r+\ ) = \frac{F(r-\ )\,h_i(r-\ ) - N(r)\,w(r)\,h_{ci}(r)}{F(r-\ ) - N(r)\,w(r)} \tag{9}$$

$$h_o(r+\ ) = \frac{F(r-\ )\,h_i(r-\ ) - N(r)\,w(r)\,h_{co}(r)}{F(r-\ ) - N(r)\,w(r)} \tag{10}$$

Here h_{ci} is the enthalpy of the flow that enters the axial channels from the inlet header, h_{co} is the local axial channel exit enthalpy. N is the number of axial channels at this particular radius and w is the axial channel flow rate. The enthalpy of the fluid that enters the axial channels is assumed to be equal to the enthalpy of the inlet header, so Equation 9 predicts no discontinuity in the inlet header enthalpy.

4. Boundary Conditions

The two header pressures are two of the five boundary conditions required by the model. The others are the cryogen flow rate, the inlet enthalpy and the outlet enthalpy.

It is assumed that cryogen leaves from the bottom of the storage tank at a given pressure and subcooling. Changes in the pressure level as the nitrogen is transported to the motor inlet header are ignored. However, due to heat leaks in the transport piping, its energy content is increased. The inlet enthalpy boundary condition is determined from the following energy balance:

$$h_i(r_1) = \frac{Q_p}{F(r_1)} + h_o \tag{11}$$

where:

$h_i(r_1)$	is the inlet header enthalpy evaluated at the inside radius of the header
h_o	is the enthalpy of nitrogen as it leaves the storage tank
$F(r_1)$	is the radial flow in the headers at the inside radius of the header (note that the flow evaluated at the inside radius of the header is the total flow through the motor.)
Q_p	is the heat leak into the inlet piping

The following overall energy balance is used to fix the fluid enthalpy as it exits the exit header:

$$h_o(r_1) = \frac{Q_t}{F(r_1)} + h_i(r_1) \tag{12}$$

where Q_t is the total power absorbed by the cryogen as it passes through the motor.

The cryogen flow rate is not known, however an iteration procedure is implemented (see Section 6) to determine the flow rate consistent with the boundary pressures specified.

5. Constitutive Relations

A number of constitutive relations are required to obtain a solution to the differential equation set presented above.

Outlet and inlet header slip models

The model used to describe the slip between the phases in the outlet header is presented here. This model determines the local void fraction (α) and the outlet header density for use in the outlet header momentum equation. This model can also be used for the inlet header, but as will be seen, a simpler model is sufficient there. The mixture density (ρ_o) and a mixture velocity (u_o) for the outlet header are defined as:

$$\rho_o = \alpha\rho_g + (1-\alpha)\rho_f \tag{13}$$

and

$$\rho_o u_o = \frac{F}{2\pi r\delta}. \tag{14}$$

where δ is the axial thickness of the header region. The mixture velocity is artificial but allows for a more physical understanding of the model. The mixture velocity is used to introduce the local phase velocities (u_{of} and u_{og}) via the following relation:

$$\rho_o u_o = \alpha\rho_g u_{og} + (1-\alpha)\rho_f u_{of} \tag{15}$$

In a similar manner, the outlet header enthalpy can be related to the local phase velocities:

$$\rho_o u_o h_o = \alpha\rho_g u_{og} h_g + (1-\alpha)\rho_f u_{of} h_f \tag{16}$$

The above four equations (13 through 16) cannot be solved at this point since they include five unknowns (u , ρ_o, α, u_{of} and u_{og}). The pressure (and, therefore, the saturated fluid properties), the outlet enthalpy, and the radial flow rate are assumed to be known from the solution of the governing differential equations.

To close the problem, a steady-state gas-phase momentum equation is introduced:

$$\frac{1}{r}\frac{d}{dr}(r\alpha\rho_g u_{og}^2) = -\alpha\frac{dP_o}{dr} + \alpha\rho_g\omega^2 r - I + W \tag{17}$$

The term on the left hand side of the above momentum balance is the radial acceleration term. In low quality and low pressure systems this term is negligible when compared to the other terms. The first term on the right hand side of Equation (17) can be determined from the mixture momentum equation (Equation 4). The second term on the right-hand side of Equation (17) is the centripetal acceleration of the gas-phase. The last two terms on the right-hand side of Equation (17) represent the interfacial drag between the liquid and the gas-phases and the wall drag. The wall drag term is ignored, which is consistent with ignoring it in the header mixture momentum equations (Equations 3 and 4). The interfacial drag term can be written as a function of the relative velocity between the phases. We assume that the gas-phase exists as bubbles with diameters (D_b) on the order of the axial channel size. The following relation was derived by Rivard and Torrey (1975):

$$I = \frac{3}{4}\rho_o\left[C_d|u_{og} - u_{of}| + \frac{24\nu_o}{D_b}\right]\left[\frac{\alpha}{D_b}(u_{og} - u_{of})\right]. \tag{18}$$

The following functional form for the drag coefficient of a spherical bubble is used (Bird, et al., 1966). This is based on the bubble Reynolds number (Re_b):

$$C_d = 0.44 \quad for \quad Re_b = \frac{(u_g - u_f)\rho_f D_b}{\mu_f} > 500 \tag{19}$$

$$C_d = \frac{18.5}{(Re_b)^{0.6}} \quad for \quad 1.9 < Re_b < 500 \tag{20}$$

$$C_d = \frac{24}{Re_b} \quad for \quad 0.1 < Re_b < 1.9 \tag{21}$$

$$C_d = 240 \quad for \quad Re_b < 0.1 \tag{22}$$

By solving Equations 13 through 18 simultaneously at each radial location, the local void fraction (and thus density) can be found. This is then used in the outlet momentum equation to establish the radial pressure gradient. Small void fractions are obtained since the large centripetal acceleration results in large vapor velocities toward the central exit relative to the liquid velocity.

A completely analogous method was tried for the inlet header. However, in the inlet header, vapor is produced at small radii (due to local boiling and vapor supplied via the inlet line), and cannot leave except through the axial channels. The liquid portion of the incoming flow is strongly accelerated towards the outer radii, leaving the vapor behind. Thus, a droplet flow regime is expected. Therefore, Equation (18) is replaced by a droplet correlation for the interfacial drag. The code predicted void fractions for the inlet header at small radii to be very close to one (>0.999), which made the local density very close to the vapor density. Therefore, in this region, the inlet header radial pressure gradient was small (when compared to the gradient in the exit header).

The slip model for the inlet header showed that the void fraction changed quickly to zero at larger radii where the quality becomes negative (here the definition of quality is $x_i = (h_i - h_f) / (h_g - h_f)$). The extra accuracy obtained by including a slip model for the inlet header came at a large computational cost of determining the inlet void fraction, and the model results were not sensitive to the resulting small changes in the inlet header density. Thus, a simpler model is introduced that produces calculational results indistinguishable from the more complex model. The inlet void fraction is set to 0.9999 while the quality of the flow was greater than zero, and to zero when the flow becomes subcooled (or the quality becomes negative). At the lower radii, where the void fraction is high, the inlet conditions for the axial channels is assumed to be saturated vapor. After the inlet quality becomes negative (which happens relatively fast due to the loss of vapor via the axial channels), the axial channels are fed with the liquid in the inlet header. This model for the channel inlet enthalpy seems very reasonable. The liquid experiences the large radial velocities, and makes up such a small fraction of the volume, it is unlikely that much will turn 90 degrees and enter an axial channel at the lower radii.

Axial channel flow constitutive model

The flow rate, w, through a channel is obtained by searching for a match between the total pressure loss through the channel and the imposed pressure drop. This search is complicated by the fact that Ledinegg instabilities (Bergles, 1981) may exist, and therefore, more than one match is possible. The code attempts to determine all three solutions when they exist. The results presented later include inlet orifices that have a orifice coefficient (K) of 10. These orifices can be sized to remove the possibility of Ledinegg instabilities for channels that experience boiling flow (near the center) and to limit the flow of cryogen in regions of low heat load or high driving pressure differential.

The pressure drop across a single channel is divided into four terms. These are the orifice pressure drop, the single-phase region frictional pressure drop, the two-phase region frictional pressure drop, and the acceleration pressure drop. The equations used for each are presented below:

$$\Delta P_{entrance} = \frac{K(w/A)^2}{\rho_f} \qquad (23)$$

$$\Delta P_{\phi_1} = \frac{2 f_{\phi_1} L_{\phi_1} (w/A)^2}{D \rho_f} \qquad (24)$$

$$\Delta P_{\phi_2} = \int_{L_{\phi_1}}^{L} \frac{2f_{\phi_1}(w/A)^2}{D\rho_f}(1 + x_c v_{fg}\rho_f)\left(1 + x_c\left(\frac{\mu_f - \mu_g}{\mu_g}\right)\right)^{1/4} ds \qquad (25)$$

$$\Delta P_{acceleration} = (w/A)^2 x_c v_{fg}. \qquad (26)$$

The frictional pressure drop model in the two-phase region is the one presented by Collier (1981). It has an identical form to the frictional pressure drop in the single-phase region but includes an additional term (often called a two-phase multiplier) to account for the increased velocity and turbulence in the two-phase region. This model is recommended for low-quality flows, like this application. A number of different models were tried for the two-phase frictional pressure drop before the Collier model was chosen. The calculated flow varied by an order of magnitude between the lowest and the highest predicted values. This points out the necessity of an experimental program to help define the flow rates in this particular application. Most of the correlations for the various models were developed for steam/water or air/water flows in 1-g fields. The present application is significantly different since the large acceleration field may result in more stratification of the flow. In the numerical representation of the rotor, the axial channels are divided into 20 elements to enable the approximation of the integral in Equation (25). The enthalpy changes of the fluid as it travels axially is also determined on the same grid. The pressure and enthalpy are used to determine the cell temperature, and the exiting enthalpy is used in the exit header energy balance.

Internal Conduction within the rotor.

The rotor is divided into elements radially and axially. The radial divisions correspond to the radial locations of the axial channels. The axial divisions correspond to the axial divisions used in calculating the channel flow in the previous section. The energy equation for each element includes convection to the cryogen, conduction to neighboring elements, and a heat-source term to represent electrical resistance. Currently, it is believed that the electrical resistance will result in less than 5 Watts of thermal power.

Due to the layered construction of the rotor, the conductivity of the rotor is anisotropic. To approximate this, different conductivity values are assigned for the radial and axial directions. Also, the conductivity of the combined torque tube and flux-shield region is different than the coil region.

Figure 2 shows the geometry assumed by the model. Note that the nodes at the largest radii represent the torque-tube and flux shield. They do not have any cryogen channels. These nodes also include the torque tube heat leaks (80 Watts each) and the radial heat leaks (10 W/m^2). The steady state energy balance equation for each node is given below:

$$0 = \kappa_a(T_{i+1,j} + T_{i-1,j} - 2T_{i,j}) + (\kappa_{r+}(T_{i,j+1} - T_{i,j}) + \kappa_{r-}(T_{i,j-1} - T_{i,j})) - \\ m(T_{out} - T_{in}) + S_{i,j} + l_{i,j} \qquad (27)$$

The first term accounts for conduction in the axial direction, and the next two account for conduction in the radial direction. The fourth term accounts for convection of heat away by the cryogen. The last two terms account for thermal energy generated within the node and the leakage of heat into the node. The leakage term is used to enable modeling of thermal heat leak from the torque tube.

In the outer nodes, which represent the torque tube and flux shield, the axial conduction coefficient is

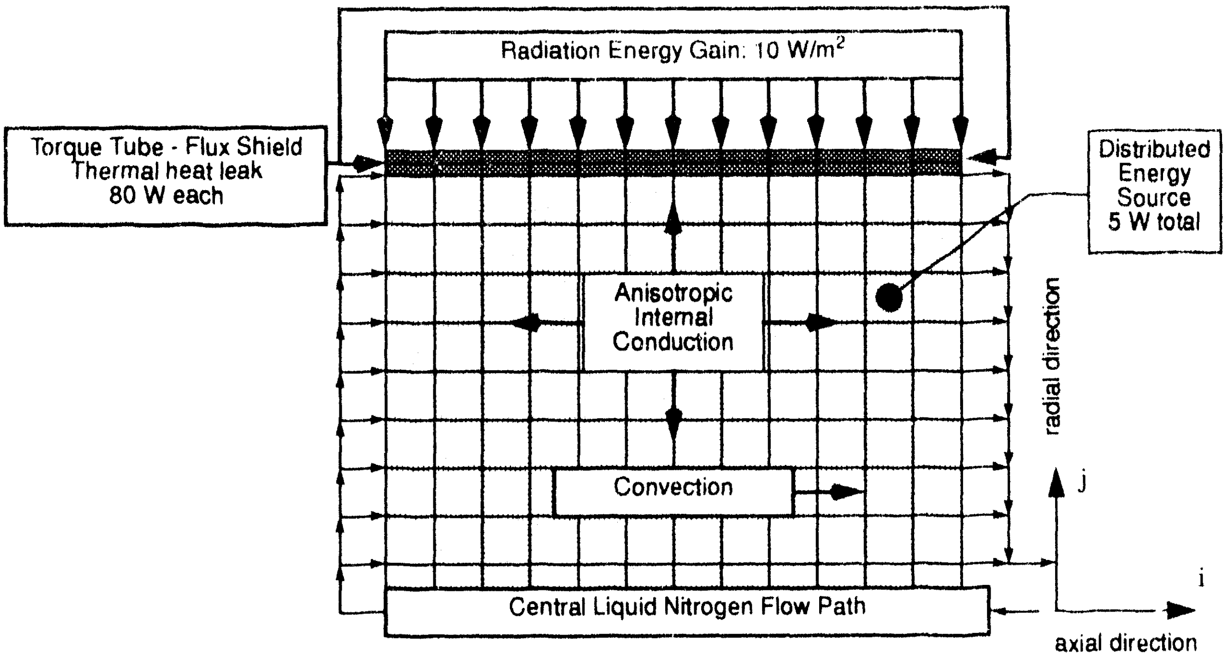

Figure 2. Nodalization of the rotor for thermal conduction. Note that the torque-tube/flux-shield nodes (shaded) include heat leaks and do not have any convective cooling.

set to 480 W/m-K to account for axial conduction through the copper flux shield. The radial conduction coefficient is set to 7 W/m-K to account for radial conduction through the stainless-steel torque tube.

Conductivity values inside the rotor are more difficult to estimate due to the layered construction. The layers are not axially symmetric, so some approximation is required. The next section summarizes our efforts in determining the conductivities that best simulate the internal conduction of heat inside of the torque tube.

It is assumed that the temperature in the model represents both the cryogen temperature and the solid temperature. (There will be a small difference between the solid and cryogen temperatures, and the sign of the difference will depend upon the heat transfer direction.) As will be seen, some nodes gain heat from the cryogen coolant.

Effective conductivity of rotor HTS region

The material properties used in this analysis are listed in Table 1. The stainless steel and silver thermal conductivities were taken from the Department 1513 thermal property material database and the encapsulation properties were supplied by Reliance Electric. The varnish is assumed to have the same thermal conductivity as the encapsulation.

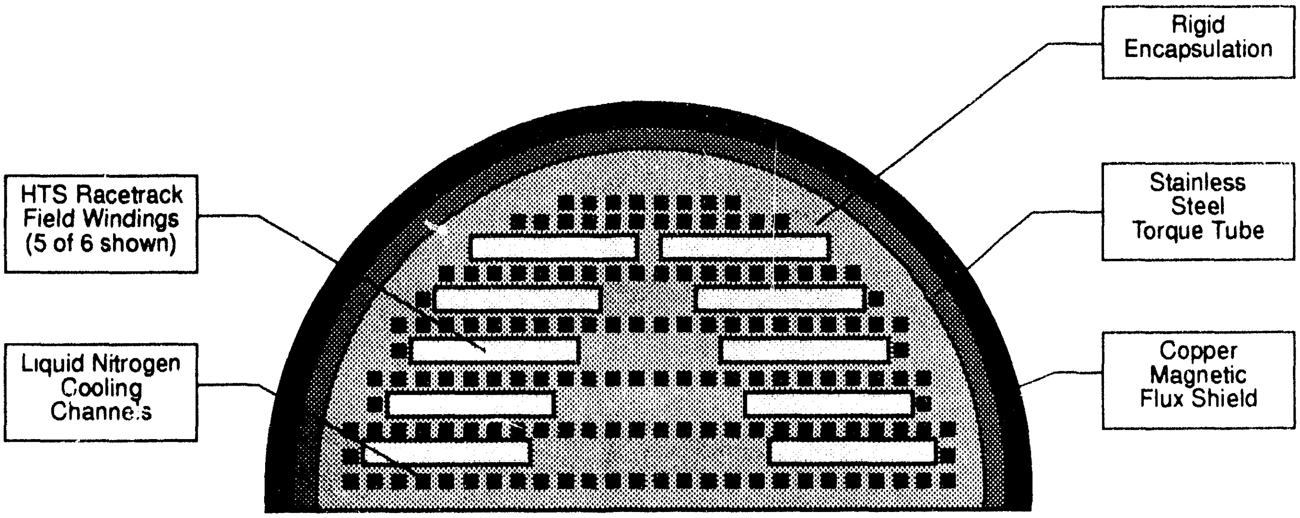

Figure 3. Radial Cross-sectional view of HTS motor showing racetrack coils and cryogen channels (not to scale).

Table 1: HTS Motor Thermal Properties

Material	Temperature (K)	Thermal Conductivity (W/[m-K])
Silver	295	396
Stainless Steel 304	73	6.9
Stainless Steel 304	173	10.9
Stainless Steel 304	273	13.4
Stainless Steel 304	373	16.3
Rigid Encapsulation	295	0.346
HTS Wire	295	2.6
Coil Matrix, x-direction	295	5.2
Coil Matrix, y-direction	295	6.25

Each racetrack coil consists of a rectangular tape (or wire) wound in an oval, racetrack fashion. The tape section is constructed of a central rectangular superconductor wire surrounded by silver. There is a 5 mil varnish coating between tapes. The oval tapes are stacked in four layers with each layer separated by a 10 mil thickness of varnish. Each stack of tapes is encapsulated with an insulating material to form a racetrack coil. Figure 3 schematically shows how the racetrack coils are placed within the rotor. The cooling channels are machined into the epoxy surface layer of the racetrack coil every 1.5

cm. The cooling channel is formed by stacking the racetrack coils. Several modules are assembled to form the rotor of the HTS motor.

First we estimated the effective thermal conductivity of an individual HTS tape surrounded by the insulating varnish layers. This is the basic unit of the racetrack coil. Each racetrack coil (shown in Figure 3) is 4 tapes high and many tapes wide. Horizontal (x-direction) and vertical (y-direction) thermal resistors of each material component in the tape cross-section were combined to compute the effective thermal resistance in the x- and y-directions, and these are presented at the bottom of Table 1. The thermal resistances created by the insulating varnish dominated the calculation.

The above results allows simulation of the heat flow on a scale of the racetrack coils. Heat will more easily flow through the silver clad coils and the intervening varnish layers than through the encapsulating epoxy (between the racetrack coils). However, the global model developed in this report requires a single radial conductivity for the region inside of the torque tube. At some locations (Figure 3), the plane of the racetrack coils lines up with the radial direction, however, at other locations it does not. Thus, a two-dimensional axisymmetric model cannot yield detailed thermal results. A conductivity of 5 W/m-K is used in the radial direction to approximate the radial heat transfer within the rotor. This is representative of the conductivity of the racetrack coil.

The superconductors form long loops through the rotor. Except near the ends, they run axially. Since the superconductors are surrounded with silver, the tapes form low-resistance paths for axial conduction of heat. The axial thermal conductivity in the rotor is set to 245 W/m-K. This represents approximately 55 percent of silver conductivity (or the volume fraction of silver). The axial value is significantly higher than the radial since the heat does not have to travel through any insulating varnish layers in the axial direction.

Cryogen properties

An equation of state is now needed to enable a solution. A detailed correlation for nitrogen properties was obtained from the Center for Applied Thermodynamic Studies at the University of Idaho, Moscow, Idaho. This was found to be accurate to within 0.1 percent of experimental data. It was provided in Fortran and was incorporated with the above equation set.

6. Solution Technique

To start the procedure, the exit pressure, $P_0(r_1)$, is assumed. With the initial conditions for all of the state variables either given, calculated, or assumed, the equation set is integrated towards the radial location of the outer most axial channels. The equation set becomes singular at the maximum radius (where the radial flow in the headers goes to zero). However, at the radius equal to the location of the last axial channels the integration is stopped. The updated axial channel flow rates are summed to obtain a new total flow rate for the next iteration.

To solve the axial flow equations coupled with the conduction equations, an iterative technique was developed. Initially the temperature and flow distribution within the rotor is guessed. The actual values of the guess are not of great concern, however, guessing flows through the axial channels that are higher than expected seems to enable more rapid convergence than lower flows. The previous temperature solution is used to generate conduction fluxes between nodes. The conduction fluxes are then added to the source term (in Equation 27), to calculate thermal loads for the next iteration. The axial flow rates, temperature distribution, and the thermal fluxes are updated in each iteration in an under-relaxed manner. Under-relaxation was found to enable an orderly progression towards the steady state solution and reduced computational time. In fact, without under-relaxation, some conditions would not yield a converged solution.

During a single iteration, the old flow rate for each axial channel group (at a prescribed radius) is used along with the current inlet header pressure in the axial channel flow and heat removal constitutive relations (Equations 23 through 27). As the equations are integrated across the rotor, a new temperature field is predicted. However, with the under-relaxation, the new temperature for each node in succession (from inlet header to outlet header) is obtained from the following formula:

$$T_{i,j}^{new} = s_1 T_{i,j}^{pre} + (1 - s_1)\, T_{i,j}^{old} \tag{28}$$

where s_1 is the under-relaxation parameter (between zero and one) for the temperature, and $T_{i,j}^{pre}$ is the temperature that would be predicted by the conservation equations given the old value of the heat flux into the node. $T_{i,j}^{new}$ and the local pressure is now used to define the fluid state entering the next axial node $(i, j+1)$ and the process is repeated. When the outlet header is reached, the fluid pressure (P_c) and enthalpy exiting the channel is obtained. The flow rate is then updated (for use in the next iteration) by the following formula:

$$w_i^{new} = s_2 w_i^{pre} \sqrt{\frac{P_i - P_o}{P_i - P_c}} + (1 - s_2)\, w_i^{old} \tag{29}$$

As the flow approaches its correct value, the square root term in the above equation becomes unity, and the flow rate converges.

Finally, after the iteration is completed, the thermal conduction fluxes are calculated for each of the nodes using the updated temperature distribution. These fluxes are also under-relaxed:

$$q_{i,j}^{new} = s_3 q_{i,j}^{pre} + (1 - s_3)\, q_{i,j}^{old} \tag{30}$$

These under-relaxed relations simulate inertia. The under-relaxation of the temperature simulates the inertia of the thermal mass of the rotor in a transient and the under-relaxation of the flow equation simulates the momentum of the flow. However, there is no physical analogy for the under-relaxation of the heat flux terms. However, this has proved necessary to obtain converged solutions. This simulation of inertia is why such solution schemes are called false transients.

The individual under-relaxation parameters may be individually specified. No effort has been made to make them consistent with their physical inertial analogies.

7. Model Results

Model results are presented in the following figures. Figure 4 shows the conductor power density within the rotor. It is assumed that the superconducting wire provides a loss of 5 watts, and this loss is distributed within the rotor in proportion to the local wire density. In future versions of this model it is hoped to include local temperature and magnetic field effects on the resistance of the wire to enable a more accurate distribution of the electrical losses. However the electrical losses are small when compared to the thermal heat leaks. The rotational velocity of the rotor was chosen to be 3600 rpm, but some results for 1800 rpm are presented for comparison. Table 2 summarizes the various heat leaks assumed in the simulation presented here. The heat leak values are based on calculations performed by Reliance Electric. The outlet header heat leak is significantly greater than the inlet header due to the existence of the electrical leads in the outlet header.

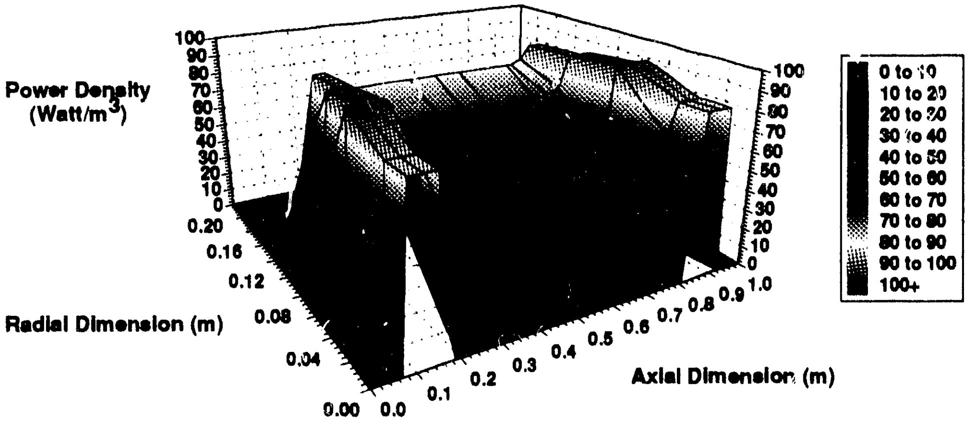

Figure 4. Thermal gain of superconducting wire (I^2R losses) within the rotor as a function of radius and length.

Table 2: Thermal Source Terms

Heat Leak	Watts
I^2R gain	5
Radiation (radial gap)	14
Conduction (Inlet header)	3.5
Conduction (Outlet header)	17.5
Conduction (Feed tube)	30
Conduction (Torque tube)	160
TOTAL	230

Table 3 presents the location of the axial cooling channels used to model the rotor. The number of channels at each radii is obtained from preliminary design drawings provided by Reliance Electric. Note that at the higher radii, more channels are required to maintain a constant channel density. The size of the channels is reduced at the higher radii where the pressure drop across the channels becomes larger.

Table 4 presents the boundary conditions used for the example calculation presented here.

Table 3: Axial Channel Density and Size Variation

Set Number	Radial Position (mm)	Number of Channels	Channel Cross-Sectional Area (mm^2)
1	30	4	1
2	40	8	1
3	50	8	1
4	60	16	1
5	70	16	1
6	80	16	1
7	90	24	0.5
8	100	20	0.5
9	110	24	0.5
10	120	28	0.5
11	130	28	0.5
12	140	32	0.5
13	150	32	0.25
14	160	32	0.25
15	170	40	0.25
16	180	44	0.25
17	190	84	0.25

Table 4: Boundary Conditions

Inlet Pressure	1.15 atm.
Outlet Pressure	1.10 atm.
Inlet Quality	-0.01
Total Electrical Losses	5 W
Axial channel entrance K	10

The total flow rate of nitrogen through the motor was found to be 0.095 kg/s. The rotational motion of the rotor will induce a flow rate even if no overall pressure drop is imposed. This is because the density of the fluid in the outlet header will always be less then the density of the fluid in the inlet header. The minimum flow rate for this thermal power distribution and 3600 rpm was found to be approximately 0.085 Kg/s. Figure 5 shows the pressure variation in the two headers. On this scale, the inlet header and outlet header pressure variations seem identical. However, due to slightly larger fluid densities in the inlet header, the increases in the inlet header are somewhat larger. Therefore, there is an increase, with radial location, in the pressure differential between the headers. This results in the self pumping nature of the rotor. To maintain more uniform flow, axial channels are made smaller at larger radii.

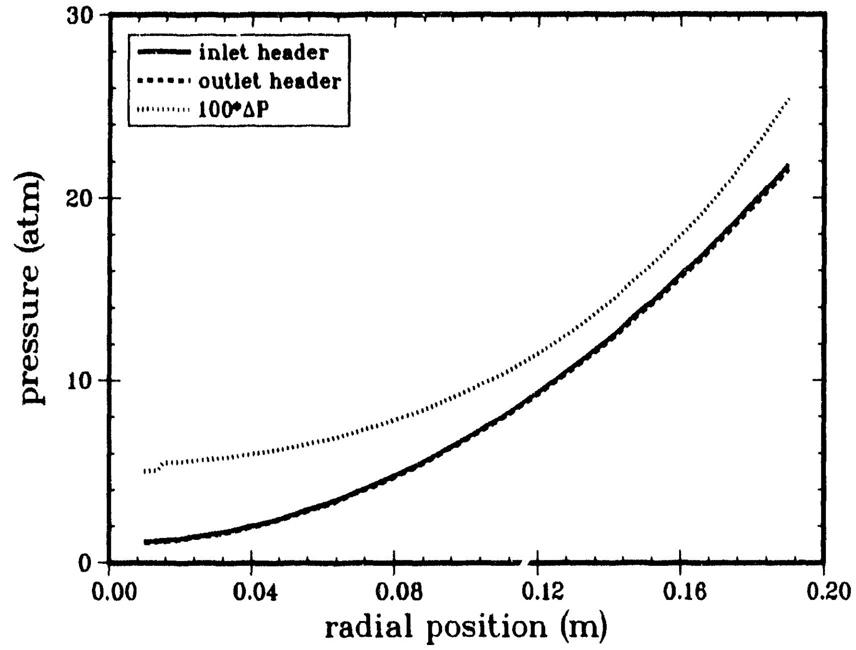

Figure 5. Radial pressure distribution in the inlet and outlet headers at 3600 rpm. 100 times the pressure difference between the inlet and outlet header is also plotted. The differential pressure increases over the radius of the rotor.

Figure 6 shows how changing the rotational speed of the rotor can strongly change the pressure profiles in the rotor. At 1800 rpm, the centripetal acceleration is less, and therefore, the pressure gradients are also less. The lower pressure levels results in two significant changes in the cryogenic flow within the rotor. First, the lower pressure at 1800 rpm results in more boiling of the liquid nitrogen. The two phase region extends out to a larger radii. Second, the lower radial pressure gradient results in lower differences between the inlet and outlet header pressures. This results in a lower self pumping effect. At 1800 rpm, the total nitrogen flow reduces to 0.075 kg/sec.

From Figures 5 and 6 it is easily seen how boiling of the liquid nitrogen is suppressed at the outer radius of the rotor. The saturated nitrogen temperature at the outer radius is 117 K at 3600 rpm and 107 K at 1800 rpm.

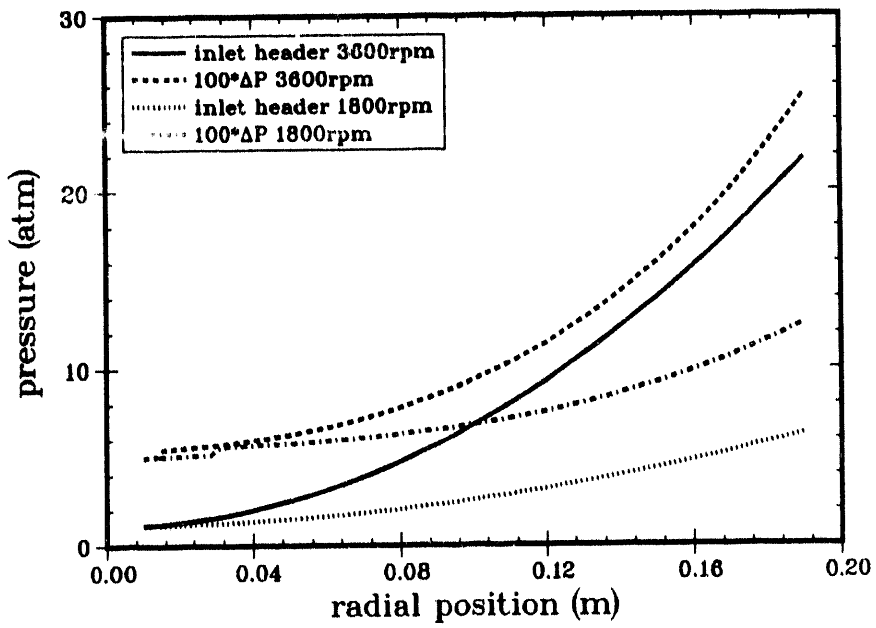

Figure 6. Comparison of radial pressure distributions and the difference between the inlet and outlet header pressures for 3600 and 1800 rpm.

Figure 7 shows the variation in the radial flow in the headers with radius. The plot starts with the total cryogen flow rate, and decreases as the radial locations of the axial channel groups are passed. The decreases become larger at larger radii where the flow per channel and the number of channels is larger. Figure 7 also shows the axial channel flow as a function of radial position. The axial channel flow tends to increase with radial position due to the increase in the difference between the two header pressures (Figure 5 or 6). However, at 0.08 and 0.14 meters, the axial channel cross-sectional area is reduced (Table 3) in order to maintain a more uniform flow distribution within the rotor.

Figure 8 shows the variation in the quality of various flows (quality is defined here as $x = (h - h_f) / (h_g - h_f)$). Due to the rapid increase in pressure, and the low power dissipation of the superconductors, positive channel exit qualities cannot be maintained. The exit header quality becomes negative (at a radial position of 16 mm). Note that the quality of the channel exit flow matches the quality of the outlet header at the radius associated with the last axial channel. The return flow in the exit header is fed by the axial channels. At the radial location of the last axial channel group, the axial flow is fed by the outer channels, and the energy (or quality) of the two flows are equal. This equality is not enforced by the numerical model during the convergence procedure. However, after the convergence has been achieved, the two qualities should be equal. This performs a check on the numerical representation of the rotor.

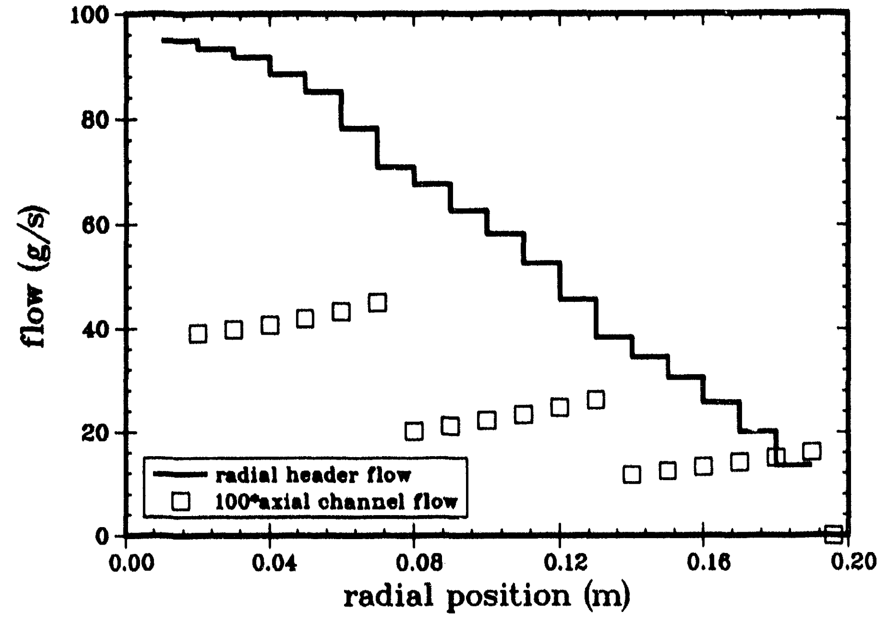

Figure 7. Radial and axial flow distribution as a function of radius in the rotor. The radial flow decreases as flow is diverted to the axial channels. The axial channels are of three different sizes, with the smaller sizes at the larger radii. This is why the axial channel flow (per channel) decreases suddenly at 0.08 and 0.14 meters (3600 rpm).

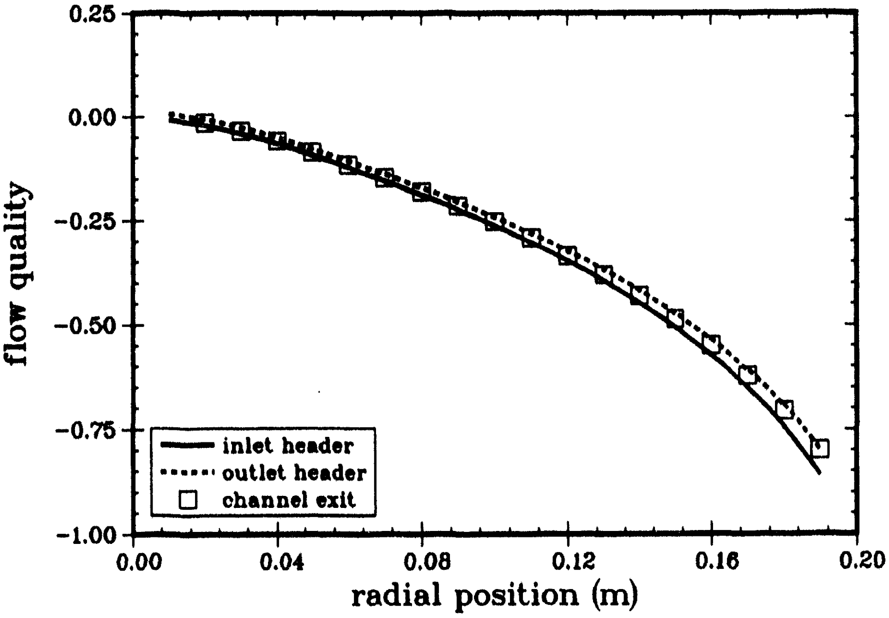

Figure 8. Variation of cryogen quality as a function of rotor radius and length. Two phase flow only exists near the center where the pressures are low (3600 rpm).

Figure 9 shows the void fractions of the axial channel exit and outlet header. Due to the large slip in the outlet header, the void fraction is much lower there than would be calculated from a no-slip model. The large slip is caused by the large radial accelerations produced by the rotation of the rotor. The large radial pressure gradient results in two-phase conditions only near the center of the outlet header. At a lower rotational speed, the two-phase region can extend farther into the header since the centripetal acceleration is smaller.

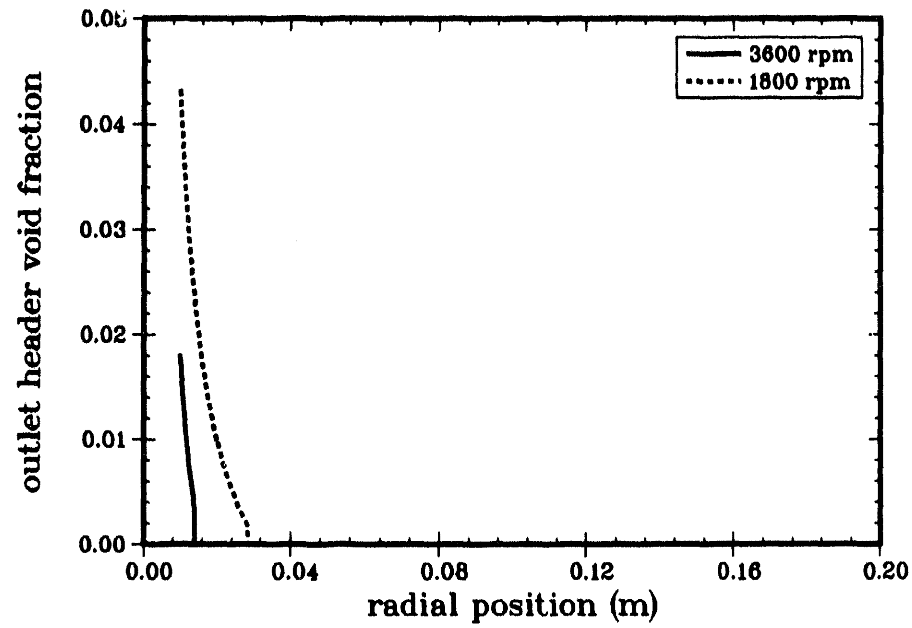

Figure 9. Variation of cryogen void fraction in the exit header for two rotational speeds.

Figure 10 shows the temperature variation of the fluid as it travels through the rotor via the axial channels. Due to the low power generated in the rotor, very little temperature change occurs. Near the attachment locations of the torque tube (Figure 2) the highest temperatures are obtained due to the concentration of the heat leak.

Figure 11 compares the numerical solutions obtained for the axial temperature distribution at the outermost channel location (0.19 m) for two different rotational speeds. This figure shows that the cryogen temperature increases sharply near the inlet header as the heat leak from the torque tube is absorbed. Then the cryogen cools as it loses heat to axial channels at lower radii. Finally, the cryogen picks up heat from the other torque tube attachment near the outlet header. As can be seen, the temperatures are slightly higher for the slower speed. This is because the flow rates become lower as the rotational speed is decreased. With the same coolant pressures applied to inlet and outlet of the rotor, the flow rate reduces from 95 grams per second at 3600 rpm, to 75 grams per second at 1800 rpm.

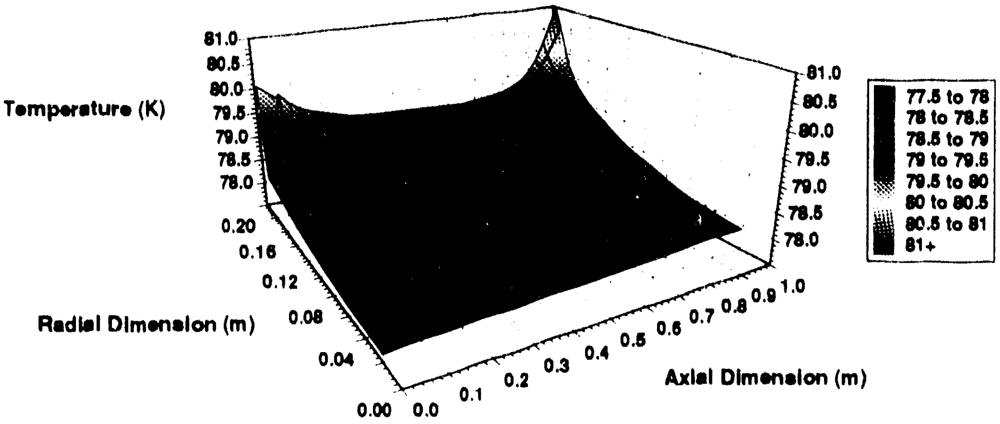

Figure 10. Contour of temperature variations within the rotor.

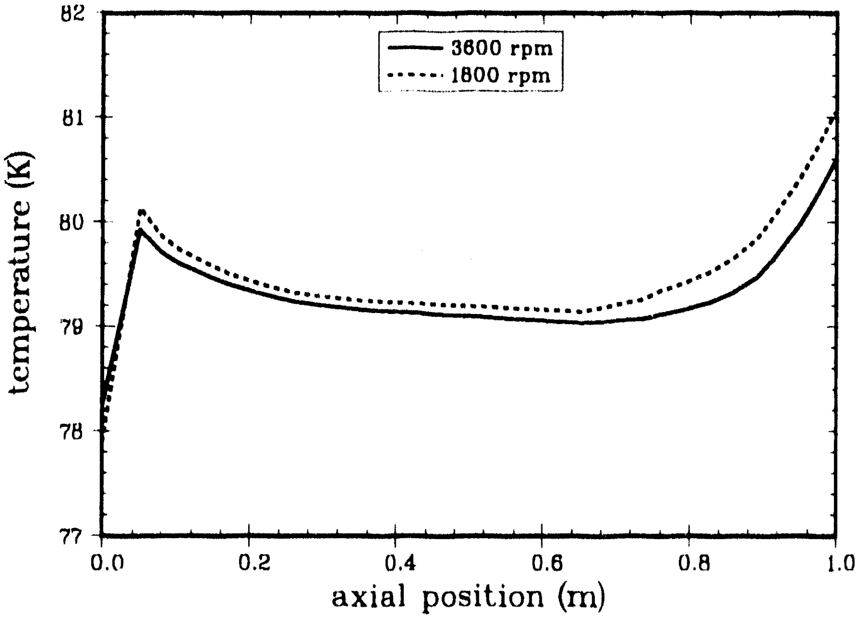

Figure 11. Axial temperature distribution at the radial location of the outermost radial channels (0.19m). Two different rotational speeds are presented.

8. Conclusions

A model has been developed to calculate the flow distribution in the rotor. The model can be used to determine the effect of changing many parameters on the fluid temperature and flow distributions. Using the low estimates for the power dissipated by the superconducting wire, little cooling capacity is needed to remove the HTS electrical losses. However, cooling channels will have to be provided for initial cool down, heat leaks, and possibly for recovery from a quench.

Due to the large radial pressure gradients that result from the large rotational speeds, one cannot rely on boiling of the nitrogen cryogen at the outer radii to maintain the temperature at 77 K. The saturated nitrogen temperature at the outer radius is 117 K at 3600 rpm and 107 K at 1800 rpm. Enough flow has to be provided to remove the thermal energy via sensible heat.This suggests that HTS materials must operate above 77 K for this application.

Both Ledinegg instabilities and density wave oscillations are possible in the geometries considered. However, boiling only occurs very near the center of the rotor, and the low power levels during steady state operation will not trigger these instabilities.

The numerical model predicts that the temperature distribution of the HTS rotor is fairly uniform due to internal conduction. A false transient solution technique was required to enable convergence for all test cases.

9. Nomenclature

A	channel flow area (m^2)
C_d	drag coefficient
D	channel hydraulic diameter (m)
D_b	bubble diameter (m)
F	the radial mass flow rate in the headers (kg/s)
f_{ϕ_1}	is a single-phase friction factor
g	gravitational constant (m/s^2)
h_e	local axial channel exit enthalpy (J/kg)
h_i	the inlet header enthalpy (J/kg)
h_o	the outlet manifold enthalpy (J/kg)
I	two phase interfacial drag term
L	total channel length (m)
$l_{i,j}$	thermal leakage into node (for connection point of torque tube) (W)
L_{ϕ_1}	single-phase channel length (m)
K	entrance friction loss coefficient
N	the number of axial channels in at a given radius
P_e	pressure at axial channel exit (converges to P_o during itteration process) (Pa)
P_i and P_o	inlet and outlet header pressure (Pa)
P_{inlet}	liquid nitrogen inlet pressure (Pa)
ΔP	axial channel pressure drop (Pa)
$q_{i,j}$	conductive thermal energy to radial location i, axial location j (W)
q''	heat flux (W/m^2)
Q	total power loss inside the motor (W)

Re_b	bubble Reynolds number
r	radial location(m)
$S_{i,j}$	Electrical loss source term (W)
s	under-relaxation parameter
t	time (s)
$T_{i,j}$	Temperature of radial location i, axial location j (K)
u_f and u_g	local liquid and gas phase velocities (m/s)
u_o	outlet header mean velocity (m/s)
v_{fg}	specific volume change upon vaporization (m^3/kg)
W	wall friction term (Pa/m)
w	mass flow through the representative channel (kg/s)
x_e	local quality of the flow exiting a channel
α	outlet header void fraction.
δ	width of the header regions (m)
κ	thermal conductance (conductivity times area divided by node spacing, (W/K)
ω	rotational speed of the rotor (rad/s)
ρ_f	saturated liquid density (Kg/m^3)
ρ_i	inlet header density (Kg/m^3)
ρ_o	outlet header density (Kg/m^3)
μ_f and μ_g	liquid and gas phase viscosity (N/sm^2)
ν_o	mixture viscosity defined as the volume weighted viscosity: $\alpha\nu_g + (1-\alpha)\nu_f$. ($m^2$/s)

10.References

Bergles, A. E., 1981, Instabilities in Two-Phase Systems, Chapter 13 of "Two-Phase and Heat Transfer in the Power and Process Industry," Hemisphere Publishing Corp.

Bird, R. B., Stewart, W. E., and Lightfoot, E. N., 1966, "Transport Phenomena," Wiley.

Collier, J. G., 1981, "Convective Boiling and Condensation," McGraw Hill.

Dykhuizen, R. C., T. C. Bickel, R. G. Baca, R. D. Skocypec, J. D. Edick, R. F. Schiferl, H. E. Jordan, Steady-state cooling of a high-temperature superconducting motor, ASME-WAM, HTD-Vol. 229, Nov. 8-13, 1992.

Greenspan, H. P., 1968, "The theory of Rotating Fluids," Cambridge.

Jordan, H. E., 1989, "Feasibility Study of Electric Motors Constructed With High-Temperature Superconducting Materials," Electric Machines and Power Systems, Vol. 16(1), pp. 15-23.

Miropolsky, Z. L., and Soziev, R. I., 1990, "Fluid Dynamics and Heat Transfer in Superconducting Equipment," Hemisphere Publishing Corp.

Rivard, W. C., and Torrey, M. C., 1975, "Numerical Calculation of Flashing from Long Pipes Using a Two-Fluid Model," LA-6104-MS, Los Alamos, NM.

Wolsky, A. M., Daniels, E. J., Giese, R. F., Harkness, J. B. L., Johnson, L. R., Rote, D. M., and Zwick, S. A., 1989, "Applied Superconductivity," Noyes Data Corporation, pp. 96-117.

Distribution

Dr. Amit DasGupta
U.S. Department of Energy
Chicago Operations Office
9800 South Cass Ave.
Argonne, IL 60439

Dr. Russell Eaton, III
U.S. Department of Energy
Forrestal Bldg., CE-32
1000 Independence Ave. SW
Washington, DC 20585

Dr. Robert McConnell
National Renewable Energy Lab
Branch 210, Location 16/3
1617 Cole Boulevard
Golden, CO 80401

Mr. Robert A. Hawsey
Oak Ridge National Laboratory MS-6040
Superconducting Technology Center
P. O. Box 2008
Oak Ridge, TN 37831-6040

Dr. David O. Welch
Bldg. 480
Brookhaven National Laboratory
Upton, NY 11973-5000

Messrs. J. Badin and C. Matzdorf
Energetics
7164 Gateway Drive
Columbia, MD 21046

Dr. James G. Daley, Jr.
U.S. Department of Energy
Forrestal Bldg., EE-14/5F-064
1000 Independence Ave. SW
Washington, DC 20585

Mr. Richard Balthasen
U.S. Department of Energy
Albuquerque Operations Office
Albuquerque, NM 87185

Mr. Dean E. Peterson
Los Alamos National Laboratory
MS-K763
P. O. Box 1663
Los Alamos, NM 87545

Dr. George O. Zimmerman, President
510 Commonwealth Ave.
Suite 355
Boston, MA 02215

Messrs. R. B. Poeppel and R. F. Giese
(2 copies)
Argonne National Laboratory
9700 South Cass Avenue
MCT/212
Argonne, IL 60439-4838

Mr. James Dirks
Battelle, Pacific Northwest Laboratories
Technology and Planning Center
P. O. Box 999
Richland, WA 99352

Dr. Susan M. Schoenung
W. J. Schafer Associates, Inc.
1120 Crane Street, #4
Menlo Park, CA 94025

AT&T
Attn: Mr. David W. Johnson, Jr.
Mr. John Plewes
Room 6D-321
600 Mountain Avenue
Murray Hill, NJ 07974

Messrs. Howard E. Jordan,
Richard F. Schiferl, D. I. Driscoll (10 copies)
Reliance Electric
24800 Tungsten Road
Cleveland Ohio 44117

Dr. Ronald L. Klein
Department of Electrical & Computer Engr.
West Virginia University
Morgantown, WV 26506-6101

Dr. Stephen B. Kuznetsov, President
Power Superconductor Appliations Co.
3110 William Pitt Way
Pittsburg, PA 15238

Internal Sandia

1002	J. E. Schirber
1103	G. A. Samara
1153	B. Moprosin
1153	T. L. Aselage
1153	B. W. Dodson
1153	E. L. Venturini
1153	M. Siegal
1500	D. J. Mcloskey
1501	C. W. Peterson, route to: 1512, 1551, 1552
1502	P. J. Hommert, route to 1511, 1553, 1554
1513	R. C. Dykhuizen (5 copies)
1513	R. D. Skocypec
1513	Dayfile
1561	H. S. Morgan, route to 1562
1810	D. W. Schaefer
1831	M. M. Karnowsky

Mr. James R. Gaines, Jr.
Superconductive Components, Inc.
1145 Chesapeake Avenue
Columbus, OH 43212

Nuclear Metals, Inc.
Attn: Mr. William T. Nachtrab
and Ms. Nancy Levoy
2229 Main Street
Concord, MA 01742

Dr. William D. Ernst
Business Development Manager
Mechanical Technology Inc.
Power Systems Division
968 Albany-Shaker Rd.
Latham, NY 12110

Dr. Wei-Kan Chu
Deputy Director of Research
University of Houston
Houston Science Center
Houston, TX 77204-5932

1832	R. J. Bourcier
1833	J. L. Jellison
1840	R. E. Loehman
1842	W. F. Hammetter
1846	J. A. Voigt
1880	M. Davis
2476	F. P. Gerstle, Jr.
2476	R. H. Moore
2476	S. Lockwood
6200	D. E. Arvizu
6204	N. J. Magnani
6213	T. C. Bickel (10 copies)
6213	R. G. Keefe
6213	E. P. Roth
6213	Dayfile
7141	Technical Library (5 copies)
7151	Technical Publications
7613-2	Document Processing for DOE/OSTI (10 copies)
8523-2	Central Technical Files (1)

DATE
FILMED

12/6/93

END